frontiers | Frontiers in Physics

TYPE Original Research
PUBLISHED 30 May 2025
DOI 10.3389/fphy.2025.1575672

OPEN ACCESS

EDITED BY
Francesco Barile,
University of Bari Aldo Moro, Italy

REVIEWED BY
Bhartendu K. Singh,
Banaras Hindu University, India
Erika Catano-Mur,
College of William & Mary, United States

*CORRESPONDENCE
Marco Ferrero,
marco.ferrero@to.infn.it

RECEIVED 12 February 2025
ACCEPTED 28 April 2025
PUBLISHED 30 May 2025

CITATION
Ferrero M, Arcidiacono R, Cartiglia N, Lanteri L, Menzio L, Morozzi A, Moscatelli F, Mulargia R, Siviero F, White R and Sola V (2025) First study of single-event burnout in very-thin planar silicon sensors. *Front. Phys.* 13:1575672. doi: 10.3389/fphy.2025.1575672

First study of single-event burnout in very-thin planar silicon sensors

Marco Ferrero[1]*, Roberta Arcidiacono[1,2], Nicolò Cartiglia[1], Leonardo Lanteri[1,3], Luca Menzio[1,2], Arianna Morozzi[4], Francesco Moscatelli[4,5], Roberto Mulargia[3], Federico Siviero[1], Robert White[1] and Valentina Sola[1,3]

[1]Istituto Nazionale di Fisica Nucleare, Torino, Italy, [2]Dipartimento di Scienze del Farmaco, Università del Piemonte Orientale, Novara, Italy, [3]Dipartimento di Fisica, Università degli Studi di Torino, Torino, Italy, [4]Istituto Nazionale di Fisica Nucleare, Perugia, Italy, [5]CNR-Istituto Officina dei Materiali (IOM), Perugia, Italy

This paper investigates the single-event burnout (SEB) effect in thin irradiated positive-intrinsic-negative (PiN) diodes and low-gain avalanche diodes (LGAD). SEB is a destructive event triggered in silicon sensors by the passage of a high-momentum charged particle. This effect arises in planar sensors under specific conditions: a significant ionization event caused by the particle's passage and a very high electric field in the entire bulk region. The investigation of SEB was performed in two beam test campaigns: one at Deutsches Elektronen-Synchrotron (DESY) with an electron beam of 3.6 GeV/c momentum and the second at CERN with a pion and proton beam of 120 GeV/c momentum. The sensors under test had active thicknesses from 15 μm to 55 μm and active surfaces from 1.7 mm^2 to 433 mm^2. In preparation for this study, most sensors were irradiated with neutrons up to a fluence of $1{\cdot}10^{16}$ n_{eq}/cm^2. The experimental setup for the beam tests included a frame for the alignment of the sensor with six available slots, two of which were equipped with trigger boards to monitor the beam rate during the test campaigns. This frame was placed inside a cold box to operate the irradiated sensors at very high electric fields while keeping their leakage current low. The experimental results show an inversely proportional relationship between the electric field at the SEB (SEB field) and the active thickness of the sensors. In this study, the SEB field increases from 11-12 V/μm in a 55-μm-thick sensor to 14 V/μm in a 15–20 μm-thick sensor.

KEYWORDS

single-event burnout, SEB, thin silicon sensors, PiN, LGAD

1 Introduction

The low-gain avalanche diode (LGAD) technology Pellegrini et al. [1] enhances traditional silicon sensor designs by incorporating moderate internal gain (10 – 50) into the signal formation process. A key figure of merit of LGADs is their excellent temporal performance (~30 ps) in measuring the time of passage of charged particles. This precision is made possible by the combination of internal gain and thin active thickness (~50 μm) that minimizes the signal collection time. Thanks to their timing

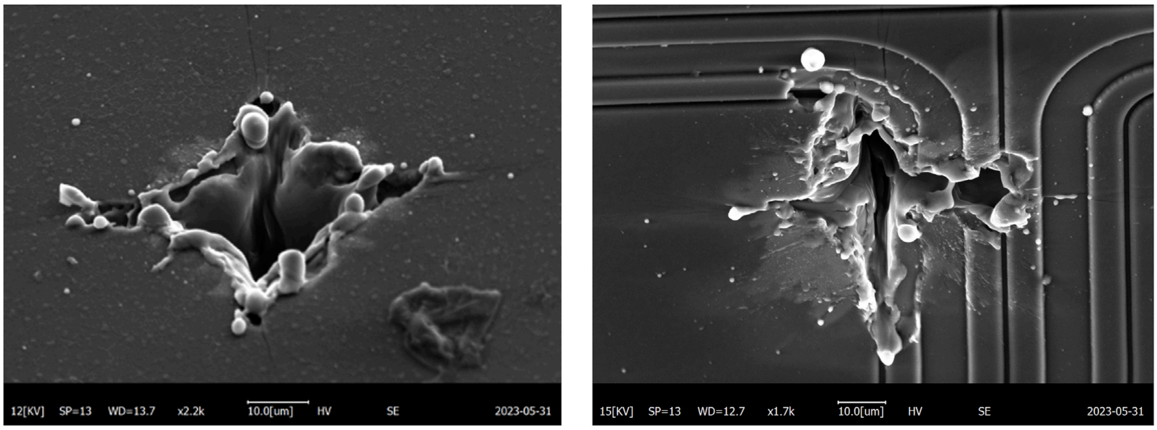

FIGURE 1
Scanning electron microscope (SEM) images of two typical SEB cross-shaped marks located in the middle of the pixel (left) and on the edge of the pixel (right). The sensors in the picture were produced by Hamamatsu Photonics (left) and Fondazione Bruno Kessler (right), with an active thickness of 50 μm (HPK) and 55 μm (FBK). The sensors were irradiated with neutrons at a fluence of 1.5· and 2.5· 10^{15} n_{eq}/cm^2, respectively. Both sensors burned out at a DESY beam test.

capabilities, LGADs have been chosen by CMS and ATLAS collaborations to instrument their timing detectors: the endcap timing layer (ETL) of the MIP timing detector (MTD) CMS [2] and the high granularity timing detector (HGTD) ATLAS [3]. One of the main challenges in the development of the LGAD technology has been maintaining unaltered performance in high-radiation environments, with particle fluences reaching 10^{15} n_{eq}/cm^2 and beyond. For these irradiation levels, the radiation damage causes the degradation of the internal gain of LGAD sensors through the acceptor removal mechanism Kramberger et al. [4]. The gain loss can be compensated by increasing the external bias applied to the device; however, the onset of destructive events at high electric fields, called single-event burnout (SEB), sets an upper limit to the maximum allowed external bias.

Investigations performed by the CMS, ATLAS, and RD50 collaborations Sola [5]; Beresford et al. [6] led to the conclusion that an SEB is triggered by the passage of a single particle when a high electric field is present in the whole volume of the sensor. The SEB mechanism hypothesis can be explained in four steps:

- A high-momentum charged particle deposits a large amount of energy, generating locally a high density of charge carriers. It is important to stress that SEB events do not happen if the momentum of the impinging charged particle is low, for example, when using a strontium-90 beta source.
- The screening effect generated by the high density of charge causes the local collapse of the electric field, leading to an increase of the electric field in the region above and/or below.
- The higher electric field triggers an uncontrolled charge avalanche multiplication that shorts the anode and the cathode together via a highly ionized channel.
- The charge stored on the sensor electrode is discharged through this channel, irreparably damaging the device.

The large amount of energy released by an SEB discharge is enough to melt the silicon lattice. The typical SEB marks are star-shaped craters located on the surface of the sensors; see Figure 1. Often, associated with the crater, two perpendicular cracks are visible on the surface, most likely running along the silicon crystal axis.

The investigations performed on 55-μm- and 50 μm-thick devices showed a clear relationship between the occurrence of SEBs and the value of the bulk electric field; for these two thicknesses, SEBs have been measured at approximately 12.7 V/μm Laštovička-Medin et al. [7], where the field has been estimated as the sensor bias over the nominal active thickness of the sensors.

2 Materials and methods

2.1 Sensors under test

The sensors tested in the beam test campaigns were manufactured by Hamamatsu Photonics (HPK) and Fondazione Bruno Kessler (FBK). These sensors are part of the second HPK and the first FBK R&D productions for the ATLAS and CMS timing detectors and the first and second FBK batch of thin sensors for the extreme fluence (eXFlu) project Sola et al. [8]; Mulargia et al. [9].

Figure 2 shows the key elements of an LGAD device. Each sensor has a pixel core and a pixel periphery. The pixel core is composed of a p^+ implant underneath an n^{++} electrode, in a p-high-resistivity bulk. The pixel periphery has an n-deep implant overlapping the electrode implant and, externally, with respect to the core, there may be another pixel or a guard ring structure, as shown in Figure 2. The guard ring consists of a double n-implant (n^{++} + n-deep), with the dual purpose of collecting the leakage current generated in the sensor periphery and preventing premature device breakdown. In between the n implants, there is a p^{++} implant, called a p-stop, for isolation purposes. An oxide layer covers the entire surface of the device. Each metal pad is DC coupled with the underlying n-implant via a metal contact through the oxide layer. A more detailed description of termination structures and their functionality can be

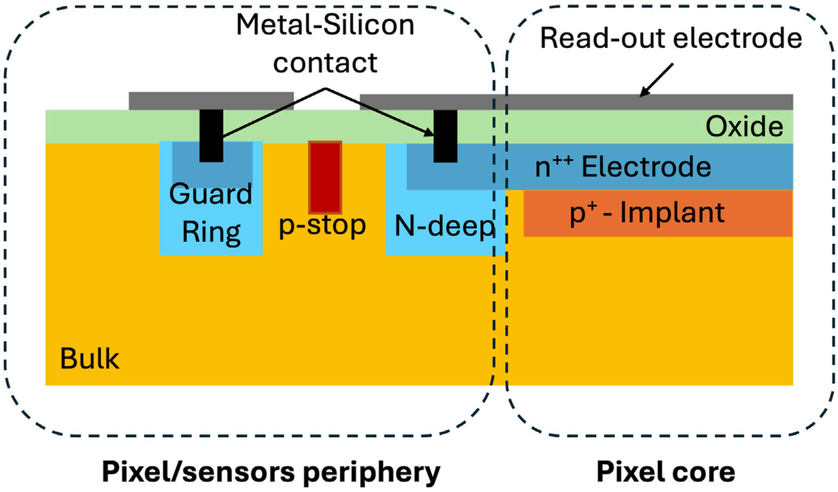

FIGURE 2
A typical cross section of an LGAD tested in the SEB campaigns. Left side: the sensor/pixel periphery composed of a guard ring and *n*-deep implants, electrically isolated from each other by a *p*-stop and both DC coupled to metal read-out electrodes through metal contacts. Right side: the pixel core composed of a p^+ implant (multiplication layer) underneath an n^{++} electrode. A PiN device is equivalent to the LGAD structure but without the multiplication layer.

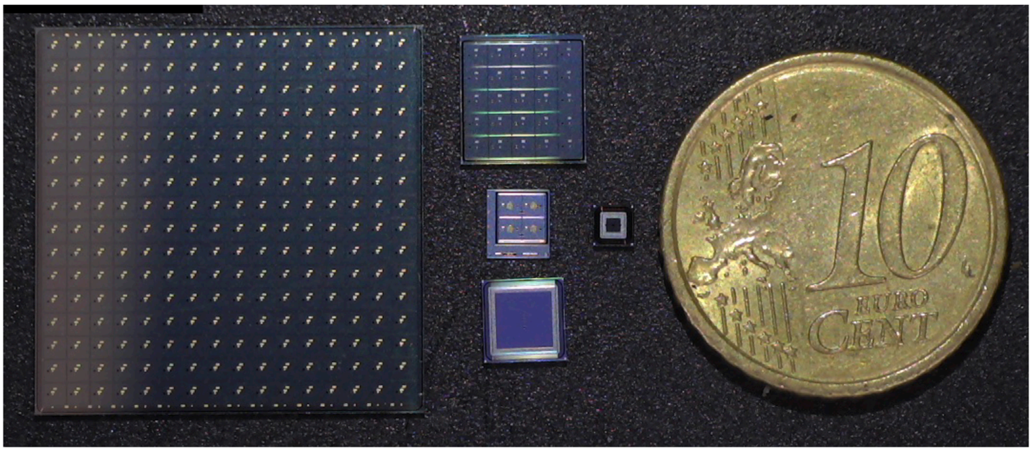

FIGURE 3
Types of sensor geometries tested during the beam test campaigns.

found in Paternoster et al. [10]. A PiN device is equivalent to an LGAD device, without the p^+ implant.

The sensors investigated in this work are un-irradiated and irradiated LGADs and PiNs and span a sizeable interval in area, thickness, and number of pixels. The thickness ranges from 15 μm to 55 μm, and the number of pixels ranges from 1 to 256. The Device Under Test (DUTs) have geometric full depletion capacitance values from 4 pF to 900 pF. Figure 3 shows a picture of DUTs with different geometries, while the full list of sensors is reported in Table 1.

The irradiation of sensors was performed at the JSI TRIGA research reactor in Ljubljana Snoj et al. [11], with neutron fluences of 1×10^{15} n_{eq}/cm^2, 2.5×10^{15} n_{eq}/cm^2, 5×10^{15} n_{eq}/cm^2, and $10{\cdot}10^{15}$ n_{eq}/cm^2. The irradiation is essential to performing an SEB study because it enables the operation of sensors above the critical electric field (E_c)[1]. Before irradiation, LGADs go into breakdown due to gain, while PiNs break down at the sensor edge below E_c.

The sensors under test also include a set of non-irradiated PiNs that are able to reach E_c before breakdown.

The wide range of geometries and irradiation levels of the sensors under test made it possible to study the relationship between the SEB and several parameters such as sensor active surface, capacitance, and active thickness.

1 E_c represents the threshold electric field inside the sensor active thickness (also defined as sensor bulk) at which the SEB is triggered by the passage of a particle.

10.3389/fphy.2025.1575672

TABLE 1 Parameters of the tested sensors. The last column reports the values of the electric fields at which the sensors burned out (E_{above}) and the highest before burnout (E_{below}).

Sensor name	Sensor geometry	Active thickness [μm]	Active surface [mm^2]	Fluence [n_{eq}/cm^2]	Tested at	E field ($E_{above}/E_{below}/E_c$) [V/μm]
FBK-UFSD4 MS9	16 × 16	55	433	$2.5 \cdot 10^{15}$	DESY	11.5/11/11.25
FBK-UFSD4 MS2	16 × 16	55	433	$2.5 \cdot 10^{15}$	DESY	12.5/12/12.25
FBK-UFSD4 W2-T9-GR3-0 4–6	5 × 5	55	43	$2.5 \cdot 10^{15}$	CERN	12/11.5/11.75
FBK-UFSD4 W2-T10-GR3-0 1–4	5 × 5	55	43	$2.5 \cdot 10^{15}$	CERN	12/11.5/11.75
FBK-UFSD4 W13-T9-GR3-0 5–6	5 × 5	55	43	$2.5 \cdot 10^{15}$	CERN	11.5/11/11.25
FBK-UFSD4 W13-T10-GR3-0 4–6	5 × 5	55	43	$2.5 \cdot 10^{15}$	CERN	11.5/11/11.25
FBK-EXFLU0-PiN W9 8–4	Single-pixel (S)	55	1.7	$1 \cdot 10^{15}$	CERN	12/11.75/11.875
FBK-EXFLU0-PiN W7 2–4	Single-pixel (S)	55	1.7	$5 \cdot 10^{15}$	CERN	12/11.75/11.875
FBK-EXFLU0-PiN W7 3–4	Single-pixel (S)	55	1.7	$1 \cdot 10^{16}$	CERN	12.5/12/12.25
HPK-HPK2 W37 P78	2 × 2	50	6.8	$1.5 \cdot 10^{15}$	DESY	12.5/12/12.25
HPK-HPK2 W28 P60	2 × 2	50	6.8	$1.5 \cdot 10^{15}$	DESY	13/12.5/12.75
HPK-HPK2 W21 P8	16 × 16	50	433	$1.5 \cdot 10^{15}$	DESY	13/12.5/12.75
HPK-HPK2 W1 P8	16 × 16	50	433	$2.5 \cdot 10^{15}$	DESY	12.5/12/12.25
HPK-HPK2 W21 P5	16 × 16	50	433	$1.5 \cdot 10^{15}$	DESY	12.5/12/12.25
FBK-EXFLU0-PiN W11 3–4	Single-pixel (S)	45	1.7	$1 \cdot 10^{15}$	CERN	13/12/12.5
FBK-EXFLU0-PiN W11 4–4	Single-pixel (S)	45	1.7	$5 \cdot 10^{15}$	CERN	12.25/12/12.125
FBK-EXFLU0-PiN W11 5–4	Single-pixel (S)	45	1.7	$1 \cdot 10^{16}$	CERN	12.5/12/12.25
FBK-EXFLU0-PiN W6 4–4 (1)	Single-pixel (S)	35	1.7	$1 \cdot 10^{15}$	CERN	13.5/12/12.75
FBK-EXFLU0- W6 9–5	Single-pixel (S)	35	1.7	$1 \cdot 10^{16}$	CERN	13.5/13/13.25
FBK-EXFLU0-PiN W6 4–4 (2)	Single-pixel (S)	35	1.7	$1 \cdot 10^{16}$	CERN	13.25/13/13.125
FBK-EXFLU1-PiN W6-S5 26-D	Single-pixel (S)	30	1.7	0	CERN	14/13/13.5
FBK-EXFLU1-PiN W6-S5 11-F	Single-pixel (L)	30	13	0	CERN	-/13.75/-

(Continued on the following page)

TABLE 1 (*Continued*) Parameters of the tested sensors. The last column reports the values of the electric fields at which the sensors burned out (E_{above})and the highest before burnout (E_{below}).

Sensor name	Sensor geometry	Active thickness [μm]	Active surface [mm^2]	Fluence [n_{eq}/cm^2]	Tested at	E field ($E_{above}/E_{below}/E_c$) [V/μm]
FBK-EXFLU0-PiN W5 3–4	Single-pixel (S)	25	1.7	$5 \cdot 10^{15}$	CERN	14/13/13.5
FBK-EXFLU1-PiN W17-S5 26-D	Single-pixel (S)	20	1.7	0	CERN	15/14/14.5
FBK-EXFLU1-PiN W17-S5 11-F	Single-pixel (L)	20	13	0	CERN	14.5/14/14.25
FBK-EXFLU1-PiN W18-S5 11-F	Single-pixel (L)	15	13	0	CERN	15/14/14.5
FBK-EXFLU1-PiN W18-S5 26-D	Single-pixel (S)	15	1.7	0	CERN	-/15/-

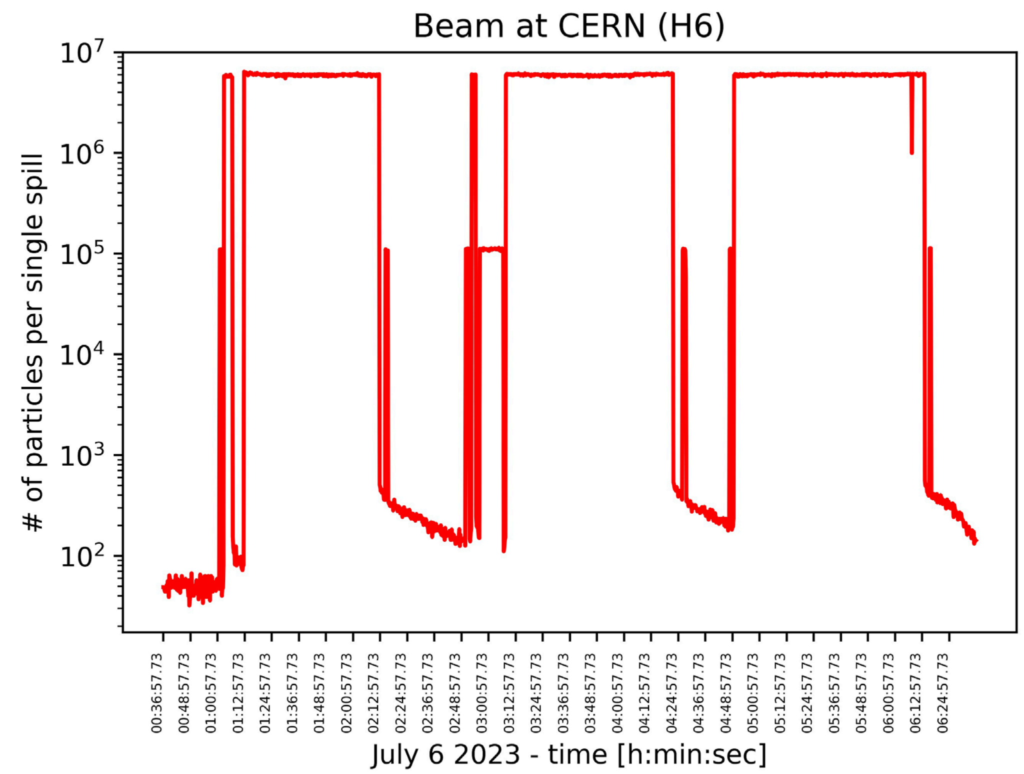

FIGURE 4
Number of particles per single beam spill monitored in a time window of 6 h during the beam test campaign at CERN. These data were extracted from CERN [13].

2.2 CERN and DESY beam test facilities and beam characteristics

The SEB investigation is based on data collected in two beam test campaigns. The first campaign was performed at the DESY beam test facility situated in Hamburg–Bahrenfeld. This facility comprises three beam lines providing electrons or positrons with selectable momenta in the range $1-6$ GeV/c Diener et al. [12]. The DESY campaign reported in this paper was conducted in the T22 experimental area. The second campaign was performed in the CERN-H6 north area with a hadron beam composed of 2/3 pions and 1/3 protons, with a momentum of 120 GeV/c. The DESY facility provides a beam with an almost continuous structure, while the CERN beam has a bunched structure. Both beams had, for the duration of the campaigns, a very good uniformity in terms of rate (particles/s $\times$ cm^2), over a transverse surface of approximately

10.3389/fphy.2025.1575672

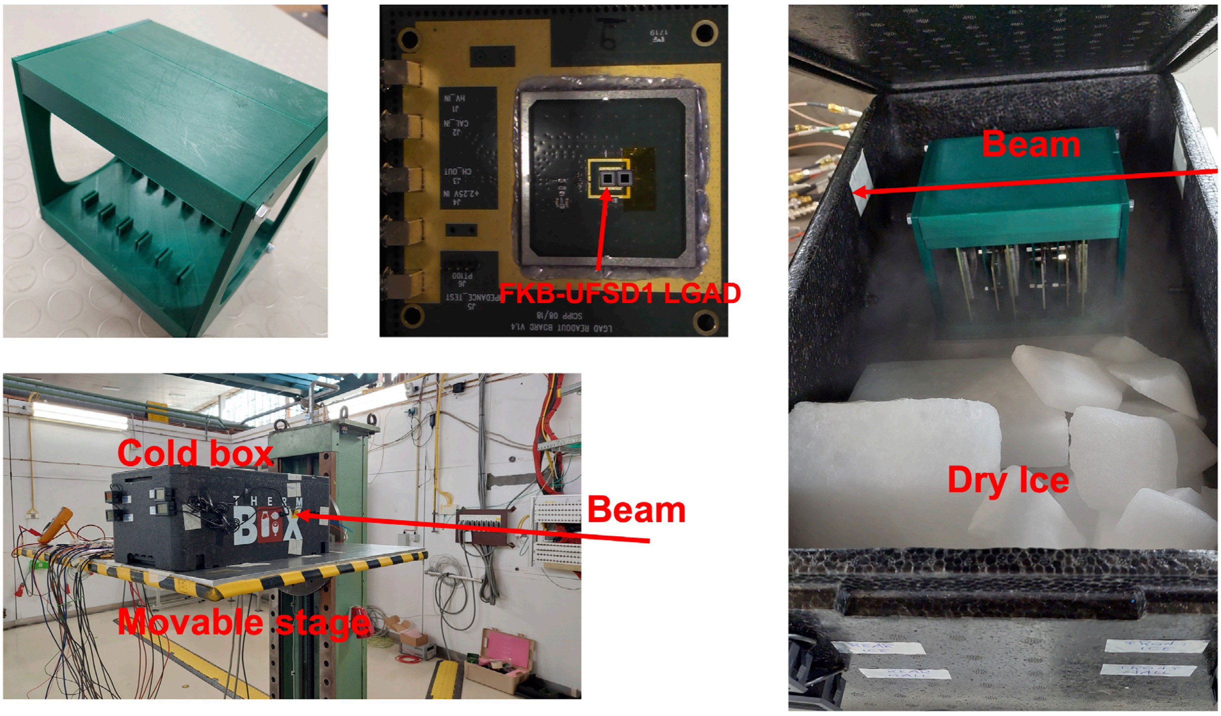

FIGURE 5
The experimental setup used at the DESY facility. Top left: Six-slot frame to support the read-out boards housing the DUTs. Top center: one of the two read-out boards with 300 μm-thick LGAD (9 mm^2) for beam monitoring. Right: Cold box with the frame holding six boards and the dry ice. Bottom: Cold box on an x-y movable stage, arranged along the beam direction.

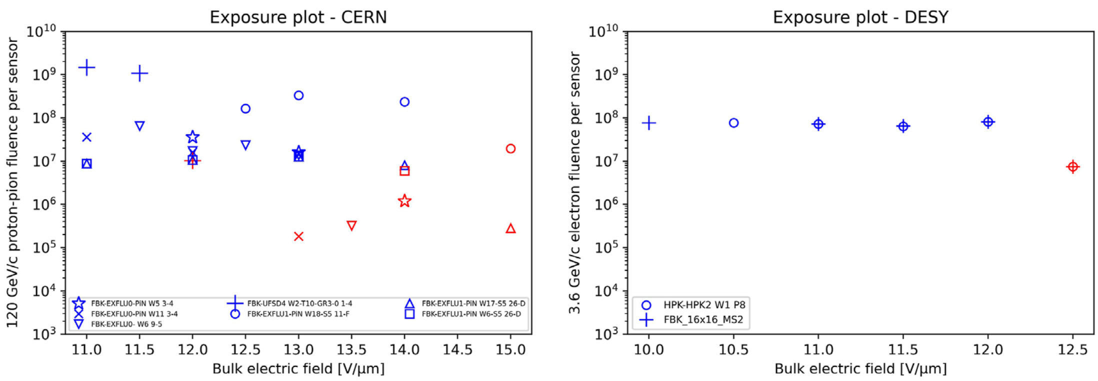

FIGURE 6
Fluence per sensor accumulated during the beam test as a function of the bulk electric field (left: CERN campaign; right: DESY campaign). Blue markers indicate the fluences and electric fields at which the sensors survived, and red markers correspond to conditions that led to burnout. Differences in fluence among the sensors are due to variations in active sensor surfaces and exposure times.

1×2 cm^2. The uniformity of the rate was verified using the beam monitoring systems available at the DESY and CERN facilities.

In DESY, the beam momentum was 3.6 GeV/c with an approximate rate of 2.5 kHz/cm^2 particles; at CERN, the intensity was higher, with an average number of particles per spill between $5.5{\cdot}10^6$ and $6.5{\cdot}10^6$. Figure 4 shows, for the CERN beam test, the number of particles per single beam spill as measured by the beam monitor scintillators over a time window of approximately 6 h. The plot shows that the rate stability was very good.

2.3 Experimental setup and sensors operations at beam tests

The sensors investigated in this work were mounted and bonded on read-out boards that provided the bias voltage to the backside of the sensor (the ohmic side) and kept all front electrodes and guard ring structures (the junction side) grounded.

To maximize the number of sensors tested simultaneously, a frame with several slots was designed and 3D printed. This frame

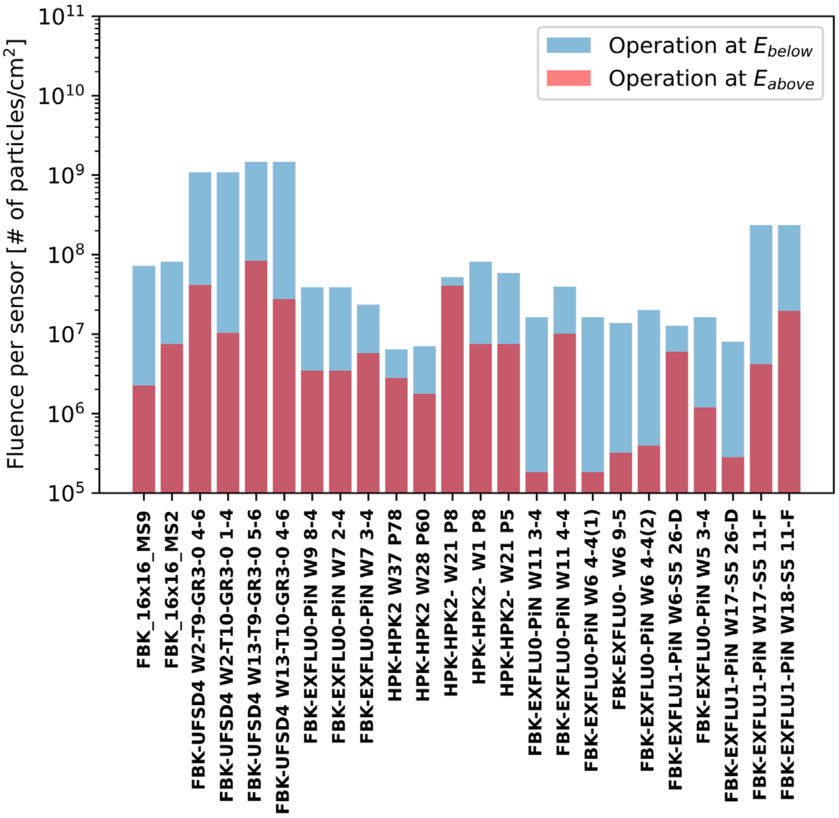

FIGURE 7
Fluence accumulated at the beam test at E_{above} (red bar) and E_{below} (blue bar) for each sensor under test. E_{below} corresponds to the highest bulk electric field at which the sensors operated without breaking, while E_{above} is the value at which SEB happened.

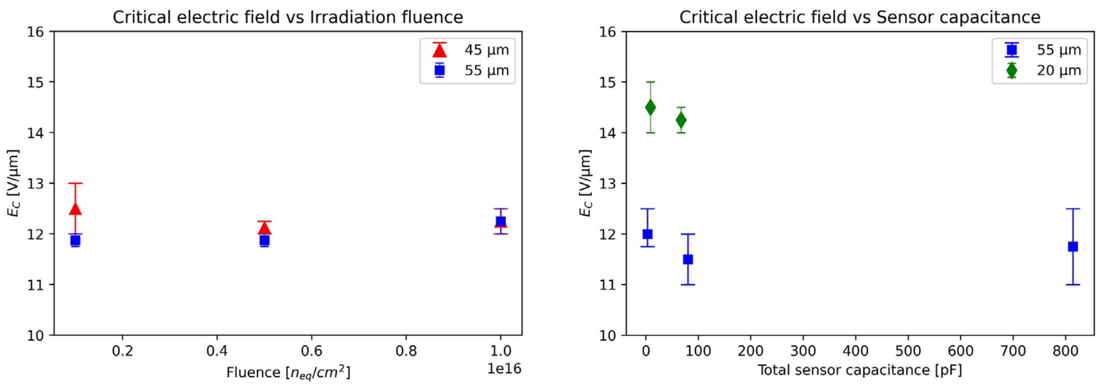

FIGURE 8
Left: average values of the critical electric field as a function of the irradiation fluence of EXFLU0 single-pad sensors with 1.3×1.3 mm^2 active area, and thickness of 45 μm and 55 μm. Right: average values of the critical electric field as a function of the sensor capacitance of single pad sensors, 2×2 and 16×16 sensor arrays, and for two different active thicknesses, 20 μm and 55 μm.

accommodated up to six read-out boards, and it ensured a good alignment between the sensors and the beam. Figure 5 (top-left) reports a picture of the frame where the boards' support fins are visible. The four central slots were used to house the sensors under test, while the two outermost slots housed sensors for monitoring the beam and the frame position.

The sensors used for beam monitoring, Figure 5 (top-center), are 300 μm-thick LGADs with a surface of 9 mm^2, from the 2016 FBK UFSD1 batch of LGADs Paternoster et al. [10]. These sensors were mounted on read-out boards developed by Santa Cruz University Cartiglia et al. [14] and provided a signal with a duration of approximately 10 ns. These sensors had the dual purpose of checking

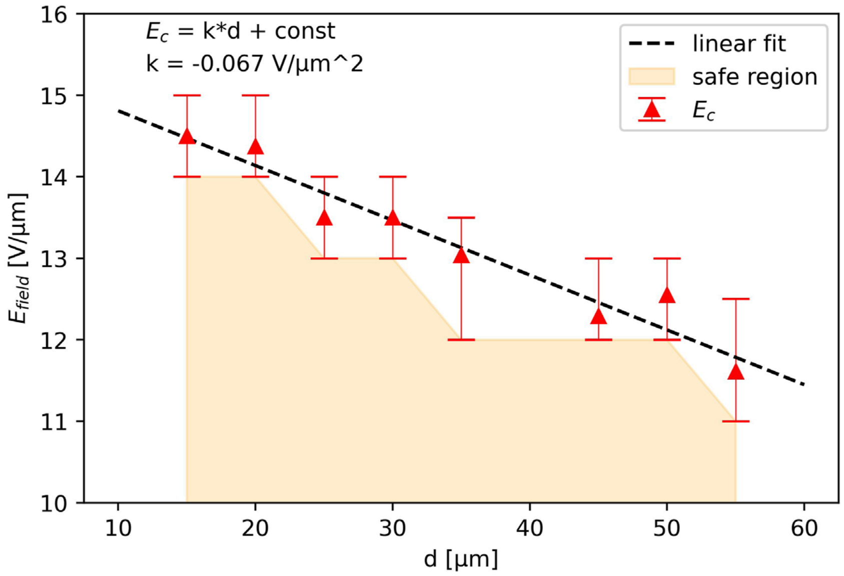

FIGURE 9
Relationship between the SEB electric field and the nominal active thickness of the sensors. The red markers correspond to the average E_c experimental data; the lower limit of the error bar, for each thickness, corresponds to the highest E_{above} and the lowest E_{below}. The dashed black line is a linear fit to the experimental data; the orange-filled area identifies the electric field region where burnout has never been observed.

the position of the frame with respect to the beam and monitoring the beam rate. These tasks were carried out for the full duration of the test by counting the particle flux.

The frame was positioned inside a hermetic polystyrene cold box. The box had a feed-through to provide the bias voltage to the sensors and to read out the monitoring devices. Solid carbon dioxide, also known as dry ice ($T = -78.5\,°C$), was used to cool the volume inside the polystyrene box. The dry ice bricks were placed in a dedicated compartment inside the polystyrene box, as shown in Figure 5 (right). An advantage of using dry ice instead of other cooling methods is that it lowers the humidity inside the box volume below 10% without needing dry air or nitrogen.

The temperature inside the box volume was monitored during all beam campaigns using PT100 sensors mounted on the read-out boards near the DUTs. The temperature was very uniform along the beam direction, ensuring the same operation conditions for all sensors inside the frame; the sensors were operated in a temperature range between −60 °C and −20 °C. Whenever the temperature exceeded −20 °C, dry ice was added. The cold box was placed on a movable stage to facilitate the alignment of the box to the beam, Figure 5 (bottom). The described setup was used at both DESY and CERN campaigns.

3 Results

3.1 Measurement methodology

During the test, the electric field was gradually increased in steps of $0.25 - 1.5\ \mathrm{V}/\mu\mathrm{m}$. After each step, the sensors were exposed to the beam for several hours (between 6 h and 10 h), and the bias was moved, in the absence of SEB, to the next step after a fluence of approximately $10^7 - 10^9$ particles/sensor. If, instead, the step would be such that E_c was reached, SEB happened quite rapidly, with a fluence below 10^7 particles/sensor. Using this experimental method, the value of E_c is determined to be between the highest value without SEB, E_{below}, and the value at which SEB has happened, E_{above}, see Equation 1:

$$E_c = \frac{E_{above} + E_{below}}{2} \pm \frac{E_{above} - E_{below}}{2} \tag{1}$$

The plots in Figure 6 (CERN beam campaign on the left, DESY on the right) report the fluence accumulated during the beam test for representative sensors as a function of the bulk electric field. The plots show that below E_{above}, SEB events do not happen even after a large fluence (blue markers) while at E_{above}, (red markers) SEB events happen rapidly, with a $10^{-5} - 10^{-7}$ probability[2], most likely correlated with the occurrence of a highly ionizing event in the silicon lattice caused by nuclear interaction between the incident particle and silicon atoms. Figure 7 illustrates this effect more clearly, showing the fluence received at E_{below} and E_{above} for each sensor.

One clear observation was that the probability of SEB occurrence did not increase with the increase in the active surface (which is linearly proportional to the capacitance) of devices exposed to the beam.

The fluences measured at CERN are underestimated by approximately 20–30% due to the saturation of the scintillator response in high-rate beam conditions, while the fluences at DESY

2 The probability is defined as 1/(particles required to induce an SEB).

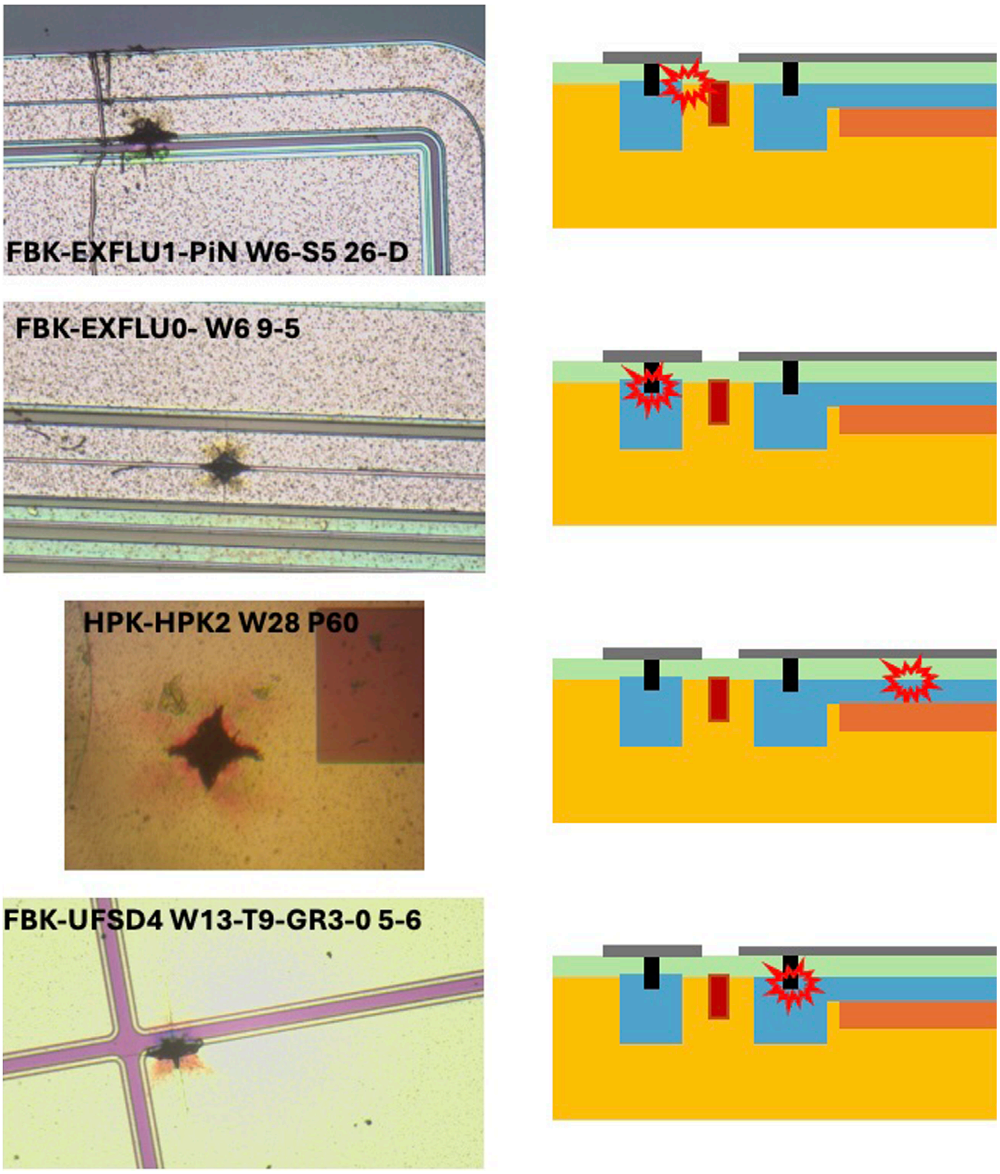

FIGURE 10
Left side: examples of craters visible in four different positions on the sensor surface. Right side: cross-section of LGADs with crater locations marked. From top to bottom, a crater on the i) guard ring edge, ii) guard ring metal contact, iii) pixel core, and iv) pixel metal contact.

TABLE 2 Positions of the crater on the surface of the sensors.

SEB crater position	Statistics
Pixel metal contact	52%
Guard ring metal contact	32%
Pixel core	8%
Guard ring edge	8%

are underestimated due to the large electron beam scattering, which generates considerable tails in the beam profile, counted by the monitoring planes but not present in the DUTs.

3.2 Parameters influencing the value of E_c

The data reported in Figure 6 and Table 1 show the burnout field values E_{above} in a wide range, between 11.5 V and 15 V/μm. To single out factors affecting SEB, the value of E_c has been studied as a function of several parameters: the fluence at which sensors have been exposed (ϕ), the sensor capacitance (C), the energy stored in the sensor capacitor ($\propto C$), and the nominal active thickness.

The average values of E_c as a function of the irradiation fluence for 45 μm- and 55 μm-thick sensors and the capacitance for 20 µm- and 55 μm-thick sensors (single pad, 2×2 and 16×16) are reported in Figure 8 left and right, respectively. The data show that the irradiation level and the sensor capacitance do not affect E_c for fixed sensor thickness. The observed variation of E_c as a function of ϕ and

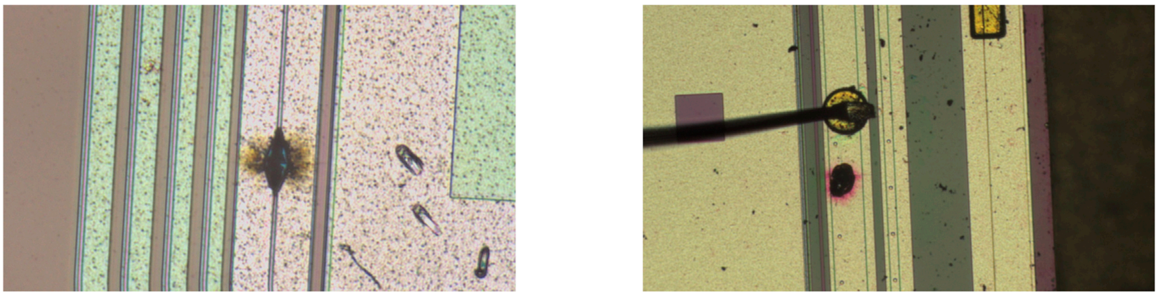

FIGURE 11
Left: crater located on a continuous contact. The line running vertically along the guard ring structure to the left of the pixel core represents the continuous metal contact; the crater (black spot) is located exactly on this line. Right: crater located on a localized circular contact. The small dots visible along the guard ring structure to the right of the pixel core correspond to circular metal contacts; in this case, the crater (the black spot with a red border) is located precisely on one of these contacts.

C are within the experimental method uncertainties, estimated as $(E_{above} - E_{below})/2$; see Equation 1.

Another factor that does not affect the SEB is the presence of the multiplication layer; both LGAD and PiN sensor types exhibited SEB at similar E_c.

A strong correlation between the sensor active thickness and E_c has been observed, as shown in Figure 9. The experimental data indicate that E_c increases linearly as d decreases, with a slope of $-0.0672 \pm 0.0067\ \mathrm{V}/\mu\mathrm{m}$, derived from the linear fit of the average E_c values reported in Figure 9. To enhance the clarity of the plot, a single average value of E_c is reported for each thickness. The associated error bars represent the range between the lowest E_{below} and the highest E_{above} measured (see the column referring to E field on Table 1). Finally, the orange-filled area shows a region of safe operation for each active thickness, where burnouts were not observed.

3.3 Optical inspection of burned-out sensors

Each burned-out sensor has been optically inspected under a microscope to locate the crater caused by the SEB. All broken sensors have a crater on the surface; in most cases, the craters have the typical cross-shape with evident breaks along the arms of the cross, as observed in previous studies: Sola [5]; Beresford et al. [6]; Laštovička-Medin et al. [7]. The craters are located in four sensor zones, as shown in Figure 10:

- edge of the guard ring, toward the pixel edge;
- metal contact on the guard ring;
- pixel core;
- metal contact on the pixel edge.

Table 2 reports the statistics for each crater's position listed above. In 84% of sensors, the burnout is located on the pad or guard ring contact; this percentage grows to 92% including the burnout on the guard ring edge; while in only 8% of sensors, the crater is located in the core of the device, away from termination structures and the periphery of the pixel.

There are several possible causes for the weakness of the pixel periphery:

1. The metal contact, locally, does not withstand the large amount of current flowing through it, causing the contact to melt.
2. The electric field in this region is higher due to the n-deep implant, which generates a deeper $n-p$ junction than in the pixel core.
3. The implants located in the pixel periphery generate a localized electric field higher than that in the bulk.

The listed hypotheses are not mutually exclusive; all of them could play a role in the SEB mechanism. Interestingly, one factor that appears to have no significant effect is the contact geometry: burnouts have been observed on both continuous and localized (circular) contacts, as shown in Figure 11, left and right, respectively.

4 Conclusion

PiN diodes and LGADs, before and after irradiation, with a wide range of capacitance and active thickness ($15\mu\ \mathrm{m} - 55\ \mu\mathrm{m}$), have been tested during two beam test campaigns at DESY and CERN to perform a comprehensive study of the SEB mechanism. The study demonstrates a strong dependence of the electric field at which SEB events happen, E_c, upon the sensor active thickness: thinner sensors can withstand higher electric fields than thicker ones. E_c decreases with a slope of $0.0672\ \mathrm{V}/\mu\mathrm{m}^2$ as a function of nominal sensor thickness in the range 15–55 μm. The study also shows that E_c does not depend upon the irradiation fluence, sensor capacitance, or area. The optical inspection of burned sensors showed the presence of star-shaped craters, mostly located on the pixel edge or the guard ring, suggesting a weakness of the peripheral pixel region, close to the contact and deep implants. Lastly, the metal contact shape between the read out and the n^{++} electrode appears to be irrelevant to the SEB mechanism.

Data availability statement

The raw data supporting the conclusions of this article will be made available by the authors, without undue reservation.

Author contributions

MF: formal analysis, visualization, investigation, writing – original draft and writing – review and editing. RA: funding acquisition, investigation, writing – original draft and writing – review and editing. NC: resources, formal analysis, writing – original draft and writing – review and editing. LL: Investigation, writing – original draft and writing – review and editing. LM: Investigation, writing – original draft and writing – review and editing. AM: Investigation, writing – original draft and writing – review and editing. FM: writing – original draft and writing – review and editing. RM: Investigation, writing – original draft and writing – review and editing. FS: Investigation, writing – original draft and writing – review and editing. RW: Investigation, writing – original draft and writing – review and editing. VS: investigation, funding acquisition, formal analysis, writing – original draft and writing – review and editing.

Funding

The author(s) declare that financial support was received for the research and/or publication of this article. This project has received funding from the European Union's Horizon Europe Research and Innovation Programme under Grant Agreements Nos 101004761 (AIDAinnova) and 101057511 (EURO-LABS). The work has been performed in collaboration with the INFN CSN5 "eXFlu" research project.

Acknowledgments

The measurements leading to these results have been performed at the Test Beam Facility at DESY Hamburg (Germany), a member of the Helmholtz Association (HGF), and at the SPS H6 Secondary Beam Line at CERN (Switzerland). The authors acknowledge CERN and DESY staff for their support during the beam test campaigns. They also acknowledge the Solid State research group of the Physics department of the University of Turin for the SEM pictures, particularly Pietro Aprà.

Conflict of interest

The authors declare that the research was conducted in the absence of any commercial or financial relationships that could be construed as a potential conflict of interest.

Generative AI statement

The author(s) declare that no Generative AI was used in the creation of this manuscript.

Publisher's note

All claims expressed in this article are solely those of the authors and do not necessarily represent those of their affiliated organizations, or those of the publisher, the editors and the reviewers. Any product that may be evaluated in this article, or claim that may be made by its manufacturer, is not guaranteed or endorsed by the publisher.

References

1. Pellegrini G, Fernández-Martínez P, Baselga M, Fleta C, Flores D, Greco V, et al. Technology developments and first measurements of Low Gain Avalanche Detectors (LGAD) for high energy physics applications. *Nucl Instr Methods Phys Res Section A: Acc Spectrometers, Detectors Associated Equipment* (2014) 765:12–6. doi:10.1016/j.nima.2014.06.008

2. CMS. A MIP timing detector for the CMS phase-2 upgrade. *Tech Rep* (2019).

3. ATLAS. Technical design report: a high-granularity timing detector for the ATLAS phase-II upgrade. *Tech Rep* (2020).

4. Kramberger G, Baselga M, Cindro V, Fernandez-Martinez P, Flores D, Galloway Z, et al. Radiation effects in low gain avalanche detectors after hadron irradiations. *J Instrumentation* (2015) 10:P07006. doi:10.1088/1748-0221/10/07/P07006

5. Sola V. Systematic study of heavily irradiated LGAD stability using the Fermilab Test Beam Facility. In: *Workshop on pico-second timing detectors for Physics* (2021).

6. Beresford LA, Boumediene DE, Castillo-García L, Corpe LD, de Sousa MJD-C-S, El-Jarrari H, et al. Destructive breakdown studies of irradiated LGADs at beam tests for the ATLAS HGTD. *J Instrumentation* (2023) 18:P07030. doi:10.1088/1748-0221/18/07/P07030

7. Laštovička-Medin G, Rebarz M, Kramberger G, Laštovička T, Andreasson J, Precek M, et al. Studies of LGAD performance limitations, single event burnout and gain suppression, with femtosecond-laser and ion beams. *Nucl Instr Methods Phys Res Section A: Acc Spectrometers, Detectors Associated Equipment* (2022) 1041:167388. doi:10.1016/j.nima.2022.167388

8. Sola V, Morozzi A, Passeri D, Siviero F, Moscatelli F, Borghi G, et al. First results from thin silicon sensors irradiated to extreme fluence. In: *PSD12: the 12th international conference on position sensitive detectors* (2021).

9. Mulargia R, Arcidiacono R, Borghi G, Boscardin M, Cartiglia N, Vignalis MC, et al. Characterization of thin carbonated LGADs after irradiation up to $2.5 \cdot 10^{15} n_{Meveq}/cm^2$. *J Instrumentation* (2024) 19:C04022. doi:10.1088/1748-0221/19/04/C04022

10. Paternoster G, Arcidiacono R, Boscardin M, Cartiglia N, Cenna F, Betta GD, et al. Developments and first measurements of ultra-fast silicon detectors produced at FBK. *J Instrumentation* (2017) 12:C02077. doi:10.1088/1748-0221/12/02/C02077

11. Snoj L, Žerovnik G, Trkov A. Computational analysis of irradiation facilities at the JSI TRIGA reactor. *Appl Radiat Isot* (2012) 70:483–8. doi:10.1016/j.apradiso.2011.11.042

12. Diener R, Dreyling-Eschweiler J, Ehrlichmann H, Gregor I, Kötz U, Krämer U, et al. The DESY II test beam facility. *Nucl Instr Methods Phys Res Section A: Acc Spectrometers, Detectors Associated Equipment* (2019) 922:265–86. doi:10.1016/j.nima.2018.11.133

13. CERN. Timber: CERN accelerator logging service (2023). Available online at: https://timber.cern.ch/. (accessed 1 July 2023 - 11 July 2023)

14. Cartiglia N, Staiano A, Sola V, Arcidiacono R, Cirio R, Cenna F, et al. Beam test results of a 16 ps timing system based on ultra-fast silicon detectors. *Nucl Instr Methods Phys Res Section A: Acc Spectrometers, Detectors Associated Equipment* (2017) 850:83–8. doi:10.1016/j.nima.2017.01.021